I&EC research
Industrial & Engineering Chemistry Research

pubs.acs.org/IECR
Article

Green Hydrogen Recovery from Natural Gas Grids by Vacuum Pressure Swing Adsorption

Lucas F. A. S. Zafanelli,* Ezzeldin Aly, Adriano Henrique, Alírio E. Rodrigues, Georges Mouchaham, and José A. C. Silva*

Cite This: *Ind. Eng. Chem. Res.* 2024, 63, 6333−6346

ABSTRACT: This study focuses on the development of a conceptual vacuum pressure swing adsorption process (VPSA) for green hydrogen (GH) recovery from natural gas grids (NGGs). Accordingly, the kinetics-based separation of H_2 from NGG was achieved by using a commercial carbon molecular sieve (CMS-3K-172) adsorbent. To develop the VPSA cycle, the CMS-3K-172 was characterized, single- and multicomponent breakthrough curves for H_2 and CH_4 were performed, and adsorption isotherms were collected between 195 and 273 K and pressures up to 18 bar. To separate H_2 (20%) from CH_4 (80%), three different VPSA cycle configurations were designed and simulated by using Aspen Adsorption. The operational variables, such as step times, intermediate-to-high-pressure ratio, purge-to-feed ratio, and H_2 initial concentration, were evaluated for maximum values of purity, recovery, and adsorbent productivity. The results show that the VPSA processes can enrich H_2 in the product stream by up to 68% with a recovery of 92%.

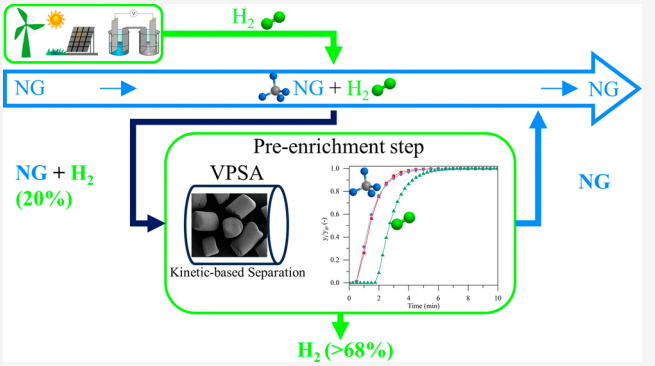

1. INTRODUCTION

Green hydrogen (GH) is widely recognized as a promising, cost-effective, and environmentally sustainable fuel due to its superior calorific value compared to other fuels, notably natural gas (141.88 MJ kg^{-1} for H_2 versus 52.21 MJ kg^{-1} for natural gas).[1,2] GH produced through water electrolysis utilizing renewable energy sources such as wind, solar, and hydroelectricity is characterized by its carbon-neutral nature. This attribute is crucial in decarbonizing the energy sector and attaining climate objectives. Furthermore, surplus renewable energy can be efficiently exploited to produce GH, enabling long-term storage and efficient transportation. Consequently, the stored GH can be employed to generate electricity during periods of high energy demand or when renewable energy supply is constrained.[1,3] Moreover, GH holds promise as a fuel for long-distance transportation, powering fuel cells in the mobility sector and helping to decarbonize heavy industries.[1,4]

The expansion of the GH sector has aroused significant interest in the scientific community regarding the establishment of a robust GH distribution network. A viable alternative approach involves the injection of GH into the existing natural gas grids (NGGs), thereby avoiding the need for extensive infrastructure investments.[5] However, upon GH injection into the NGG, it becomes important to recover and purify the GH to a high degree of purity to enable independent utilization of pure GH and NG as per the requirement. Notably, a purity level of up to 99.97% is necessary for GH to enable its conversion of electricity via fuel cells.[6,7]

Adsorption processes are widely acknowledged as economically efficient and appealing alternatives for addressing various industrial challenges, including but not limited to postcombustion CO_2 capture,[8−14] H_2 purification from steam methane reforming (SMR),[15−17] medical O_2 concentrator,[18−21] biogas upgrading,[22−25] and separation of straight-chain hydrocarbons from the branched chain.[26−29] Consequently, pressure swing adsorption (PSA), which is a cyclic process that uses pressure driven to perform bulk separation, is commonly used for H_2 purification from SMR.[16,17] The typical SMR off-gas is a mixture of $H_2/CH_4/CO/CO_2$ with a composition of 76/3/4/17%, respectively. From this composition, the conventional PSA can achieve purities of up to 99.9999% with high recoveries of around 96%.[15] However, the conventional PSA process faces challenges when applied to recovering GH from NGG due to the limited H_2 concentration, which remains an open issue in terms of admissibility, but not exceeding 20%.[6,30,31] Moreover, the high concentration of CH_4 and its

Received: December 22, 2023
Revised: February 29, 2024
Accepted: March 11, 2024
Published: March 26, 2024

https://doi.org/10.1021/acs.iecr.3c04532
Ind. Eng. Chem. Res. 2024, 63, 6333−6346

relatively weak adsorption affinity on commonly used adsorbents like zeolites, activated carbons, and silica further complicates achieving high-purity H_2 and high recovery rates.

A few studies are available in the literature that address H_2 separation from NGG by the PSA technology.[3,6,7,32−36] Liemberger et al.[35] proposed a hybrid approach involving membrane technology to initially enrich H_2, followed by further upgrading through PSA to achieve fuel cell quality as a desired concentration level. Various feed and permeate pressures as well as stage-cut (permeate flow divided by feed flow) values were examined for membrane separation. The optimized conditions for the permeate stream, set at 6 bar and 20 vol % of H_2 content balanced with CH_4, were adopted as the feed condition for the PSA step. By utilizing activated carbon as the adsorbent, the single-column PSA process achieved a high H_2 purity (>99%) along with a recovery of at least 60%.

Dehdari et al.[3] simulated a 6-bed PSA system with 12 steps to produce highly pure H_2 blended into NGG. The PSA utilized a three-layered adsorption column configuration: silica gel for capturing heavy hydrocarbons and CO_2, activated carbon for adsorbing CH_4, and LiLSX zeolite for removing trace amounts of N_2. The simulation showed that the PSA system achieved H_2 product purity exceeding 99%, with recovery rates of up to 85% for initial H_2 concentrations ranging from 5 to 30% in a 30 bar feed stream. The authors suggest additional pressure equalization steps or the use of a vacuum to enhance H_2 recovery, and experimental confirmation is necessary.

Dehdari et al.[34] conducted a comprehensive study to assess the viability of vacuum swing adsorption (VSA), a potential method for purifying H_2 from NGG at low-pressure terminals. The researchers employed a four-bed VSA apparatus filled with Norit RB4-activated carbon to achieve H_2 purity levels of 99%. The experiments were conducted with H_2 feed concentrations of 30 and 50%, balanced with CH_4, at a pressure of 102 kPa. Furthermore, the authors validated their VSA experimental data and subsequently developed a six-bed, three-layered pressure vacuum swing adsorption (PVSA) using Aspen Adsorption software. The PVSA system was predicted to achieve H_2 purity levels exceeding 99% and recovery above 93% for different initial H_2 concentrations (10−50%) at a feed pressure of 4 bar. The study also revealed that the power required to obtain H_2 purities above 99% decreased as the H_2 feed concentration and desorption vacuum increased. Additionally, the H_2 productivity was observed to increase with higher H_2 feed concentrations. Based on these findings, it can be concluded that the effectiveness of conventional processes for H_2 production is directly influenced by the initial concentration of H_2.

These studies have employed the principle of the conventional PSA process for H_2 purification, which operated based on equilibrium separation. Specifically, the process relies on the equilibrium interaction between CH_4 and the adsorbent material, while H_2, being a small and light molecule, exhibits negligible adsorption on any known material under standard temperature and pressure conditions.[32] Consequently, H_2 is selectively produced during the feed step, while CH_4 is retained within the column. However, this standard approach encounters a challenge whereby conventional adsorbents have a weak adsorption affinity for CH_4, which decreases the dynamic capacity of the fixed beds, with an impact on productivity and operational costs in conventional cyclic PSA processes. To overcome this issue, one approach involves the development or enhancement of materials with a superior CH_4 adsorption capacity compared with those existing in the literature. For example, the binder-free method has been demonstrated to enhance the adsorption capacity of zeolite by converting the binder into adsorbent matter, which leads to an adsorption increase of approximately 20%.[9,37] Alternatively, employing adsorbent materials that block or restrict the diffusion of CH_4 while also exhibiting an affinity for H_2 adsorption offers another potential solution. To the best of our knowledge, no studies have been conducted in the last direction.

Therefore, this study aims to show an adsorption process for GH recovery from NGG. For that, a conceptual vacuum pressure swing adsorption process using a carbon molecular sieve (CMS-3K-172), which kinetically separates H_2 from CH_4, is proposed and studied. Accordingly, CMS-3K-172 was characterized, single- and multicomponent breakthrough curves for H_2 and CH_4 were performed to study the dynamics of fixed-bed adsorption, and adsorption isotherms were collected. Subsequently, the breakthrough data was used to validate a fixed-bed adsorption mathematical model. After that, three different VPSA cycle configurations were designed, and simulations were performed using Aspen Adsorption software for the determination of the overall process efficiency in terms of purity, recovery, and adsorbent productivity of the H_2 final product-enriched stream.

2. EXPERIMENTAL AND METHODS

2.1. Materials. The carbon molecular sieve (CMS) 3K-172, kindly supplied by Osaka Gas Chemicals Co., Japan, consists of commercial cylindrical pellets with a diameter of 1.8 mm and a length between 1.18 and 2.8 mm. The gases employed in the study were supplied by Air Liquide Portugal with the following specifications: H_2 ALPHAGAZ 2 (99.9999%), CH_4 N35 (99.95%), He ALPHAGAZ 2 (99.9998%), and N_2 N50 (99.999%).

2.2. Characterization of CMS. The textural properties of CMS-3K-172 were assessed from the adsorption studies of CO_2 at 273 K, performed in an accelerated surface area and porosimetry system (Micrometrics' ASAP 2020) and by Hg intrusion porosimetry, performed in a pore size analyzer (Micromeritics AutoPore IV 9500). The morphology of CMS-3K-172 was evaluated by scanning electron microscopy (SEM) and high-resolution X-ray spectroscopy (EDX) using secondary electron detector (E−T). The characterization studies were performed at the Laboratorio de Solidos Porosos of Málaga University.

2.3. Fixed-Bed Adsorption and Experimental Procedure for Measuring Breakthrough Curves and Adsorption Equilibrium. Adsorption equilibrium data of pure H_2, CH_4, and their mixtures were obtained by performing a set of breakthrough curves in a cryogenic fixed-bed adsorption apparatus, developed in a previous work.[38] A detailed description of the apparatus is given in Section S1 of the Supporting Information (SI).

Single-component breakthrough experiments of CH_4 and H_2 were performed at three temperatures (195, 231, and 273 K) and pressures of up to 18 bar. Tables S1 and S2 in the SI summarize the experimental conditions for the single-component breakthrough runs for CH_4 and H_2, respectively. A binary breakthrough run was performed considering a mixture of CH_4/H_2 (80/20 vol %) at 195 K and 12 bar. The

https://doi.org/10.1021/acs.iecr.3c04532
Ind. Eng. Chem. Res. 2024, 63, 6333−6346

binary experimental conditions are summarized in Table S3 (in the SI).

2.4. Adsorption Equilibrium Model. The experimental equilibrium isotherms on CMS-3K-172 were fitted with the Langmuir model

$$q_i^* = q_{m,i}\frac{b_i p_i}{1 + b_i p_i} \tag{1}$$

where $q_{m,i}$ is the maximum adsorbed concentration of component i in mol kg^{-1}, b_i is the adsorption affinity constant of component i in bar^{-1}, and p_i is the partial pressure of component i in bar.

The effect of temperature on the adsorption affinity constant, b_i, is taken into account by the van't Hoff expression

$$b_i = b_{\infty,i}\, e^{(-\Delta H_i/RT)} \tag{2}$$

where $b_{\infty,i}$ is the pre-exponential factor of the affinity constant at an infinite temperature in bar^{-1}, R is the ideal gas constant in kJ mol^{-1} K^{-1}, $(-\Delta H_i)$ is the heat of adsorption kJ mol^{-1}, and T is the temperature in K.

The Langmuir fitting of the experimental data was carried out by a nonlinear least-squares optimization procedure in which the points were weighted according to their estimated errors

$$\sigma^2 = (1/N)\sum_{i=1}^{n}(q_i^{\exp} - q_i^{\mathrm{eq}\,(1)})^2 \tag{3}$$

2.5. Vacuum Pressure Swing Adsorption Cycle Description. The VPSA (base cycle) design configuration consists of 1 column with 5 steps per cycle, which is shown in Figure 1. The 5 steps are described as follows:

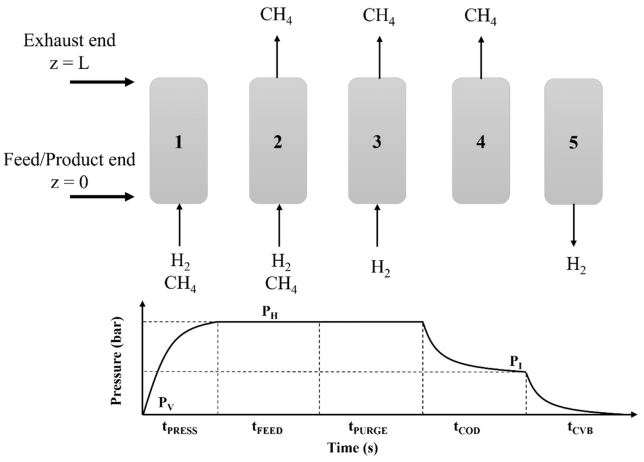

Figure 1. Conceptual VPSA cycle scheme used for H_2/CH_4 separation with CMS-3K-172. (1) Pressurization, (2) feed, (3) H_2 purge, (4) cocurrent depressurization (COD), and (5) countercurrent vacuum blowdown (CVB). P_H: high pressure; P_I: intermediate pressure; P_V: vacuum pressure.

(1) Pressurization: the column is pressurized with the feed mixture at the feed/product end (with only the feed/product end open, $z = 0$) from the vacuum pressure (P_V) to the high pressure (P_H) by t_{PRESS} seconds. As the pressure increases in the column, H_2 is adsorbed, being separated from CH_4, which spreads through the column, reaching the exhaust end, which is closed ($z = L$).

(2) Feed: the exhaust end is open ($z = L$), and the column is fed at the feed/product end ($z = 0$) at P_H with the feed mixture. In this step, H_2 is still being adsorbed, whereas CH_4 is collected at the exhaust end.

(3) H_2 purge: pure H_2 is fed at the feed/product end ($z = 0$) at P_H to purge out CH_4 located in the void spaces of the bed and adsorbent. Also, in this step, CH_4 is still continuously withdrawn at the exhaust end as a product. The H_2 purge step stream is collected from an ideal product storage tank with a purity higher than 99.97%.

(4) Cocurrent depressurization (COD): the column feed/product end is closed, and the exhaust end is kept open to cocurrently depressurize the column from P_H to an intermediate pressure (P_I) during t_{COD} seconds. This step aims to reduce the partial pressure of CH_4 in the gas phase for both adsorbent and column voids while facilitating the desorption of H_2 and consequent enrichment of its concentration along the fixed bed. Simultaneously, CH_4 is still extracted at the exhaust end with a high purity.

(5) Countercurrent vacuum blowdown (CVB): in this step, the exhaust end is closed, and the feed/product end is open to countercurrent evacuate the column from P_I until the P_V, by t_{CVB} seconds. In this step, a H_2-rich stream is collected as a concentrated product at the feed/product end of the column; at the same time, the bed is regenerated under vacuum desorption for the next cycle.

Steps (3) and (4) are both used to reduce the partial pressure of CH_4 in the gas phase for both adsorbent and column voids and enrich H_2 purity and recovery in the CVB, which is the strong adsorptive component. This strategy is well described by Yang and co-workers.[39,40] In this work, the effect of both steps (3) and (4) will be evaluated together and separately.

2.6. Performance Parameters and Parametric Study Description. To evaluate the VPSA cycle performance in terms of recovery, purity, and adsorbent productivity regarding H_2, the effect of the following process variables was parametrically studied: (i) purge-to-feed ratio (eq 4), (ii) intermediate-to-high-pressure ratio (eq 5), (iii) H_2 purge step time (t_{PURGE}), (iv) COD step time (t_{COD}), and (v) initial H_2 concentration. The purge-to-feed ratio is given by

$$P/F = \frac{\text{volume of } H_2 \text{ used in the purge step 3}}{\text{volume of gas used in the feed step 2}} \tag{4}$$

the intermediate-to-high-pressure ratio is defined by

$$P_I/P_H = \frac{\text{pressure in the COD step 4}}{\text{pressure in the feed and purge steps 1 and 2}} \tag{5}$$

The other variables were kept constant: pressurization time (t_{PRESS}) at 10 s, feed step time (t_{FEED}) at 5 s, countercurrent vacuum blowdown time (t_{CVB}) at 10 s, high pressure (P_H) at 30 bar, and vacuum pressure (P_V) at 0.1 bar. These variables were optimized for the base cycle (run 1) comprising the 5 steps VPSA and were used in all simulations.

Additionally, three different VPSA configuration cases were tested as shown in Figure 2, namely,

1) case (i) a 5-step VPSA described in Section 2.5,
2) case (ii) a 4-step VPSA without COD step 4,
3) case (iii) a 4-step VPSA without H_2 purge step 3.

https://doi.org/10.1021/acs.iecr.3c04532
Ind. Eng. Chem. Res. 2024, 63, 6333−6346

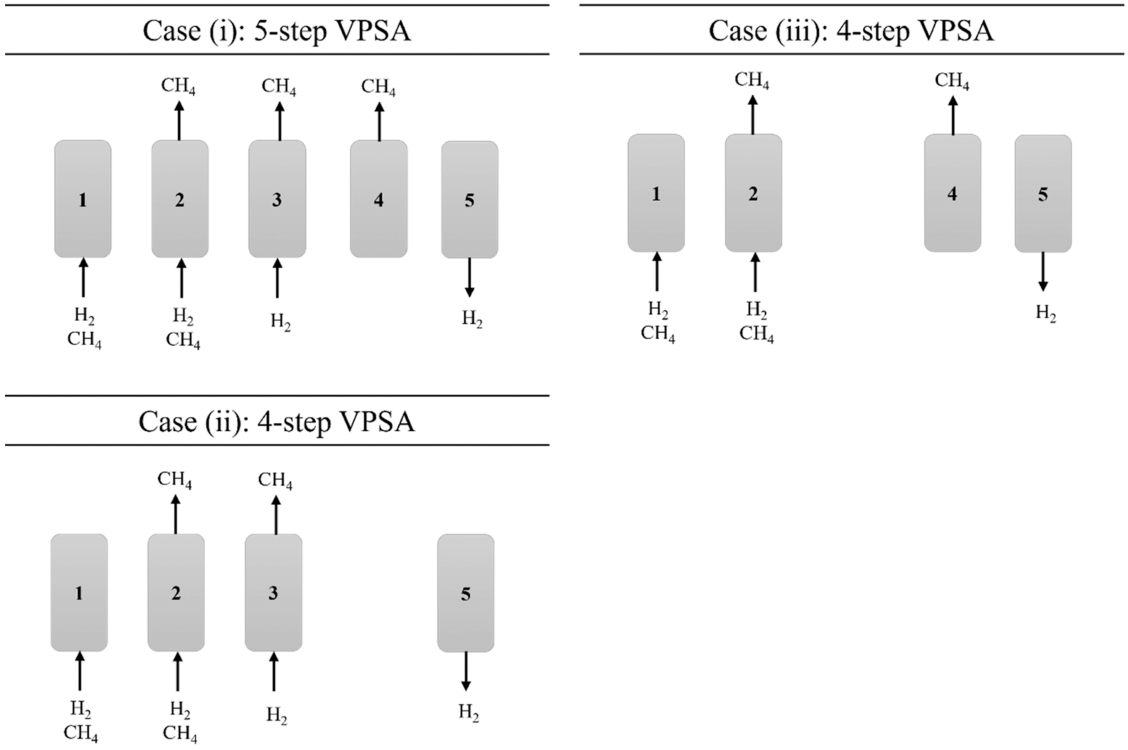

Figure 2. VPSA scheme and cyclic configurations, namely, case (i): 5-step VPSA; case (ii): 4-step VPSA (without the COD step); case (iii): 4-step VPSA (without the H_2 purge step). (1) Pressurization, (2) feed, (3) H_2 purge, (4) cocurrent depressurization (COD), and (5) countercurrent vacuum blowdown (CVB).

The parametric study includes the following studies:

- Case (i): 5-step VPSA previously described was simulated in a range of P/F and P_I/P_H different values.
- Case (ii): 4-step VPSA, without the COD step (4), was simulated to evaluate the performance by changing the P/F for different t_{PURGE} times. Accordingly, it was possible to compare the performance parameters with 5 steps versus one with only 4 steps.
- Case (iii): 4-step VPSA, without the H_2 purge step (3), was simulated to evaluate the effect of COD step time (t_{COD}) for different P_I/P_H. Accordingly, it was possible to compare it with the other cases.
- Finally, the H_2 initial concentration was changed from 20 to 30 and 50% to evaluate the effect on the best-case VPSA configuration.

The performance parameters, namely, H_2 recovery (eq 6), H_2 purity (eq 7), and adsorbent productivity (eq 8), were evaluated by the following equations

$$\text{recovery} = \frac{\int_0^{t_{CVB}} y_{H_2} F|_{z=0} dt - \int_0^{t_{PURGE}} y_{H_2} F|_{z=0} dt}{\int_0^{t_{PRESS}+t_{FEED}} y_{H_2} F|_{z=0} dt} \quad (6)$$

$$\text{purity} = \frac{\int_0^{t_{CVB}} y_{H_2} F|_{z=0} dt}{\int_0^{t_{CVB}} y_{H_2} F|_{z=0} dt + \int_0^{t_{CVB}} y_{CH_4} F|_{z=0} dt} \quad (7)$$

$$\text{productivity} = \frac{\int_0^{t_{CVB}} y_{H_2} F|_{z=0} dt}{m_{ads} \times t_{cycle}} \quad (8)$$

2.7. Mathematical Modeling and Numerical Method. The dynamic behavior of the fixed bed and VPSA can be predicted numerically based on the mass, momentum, and energy conversation laws. The mathematical model used to simulate the experimental breakthrough curves includes the effects of axial diffusion and mass transfer resistance. Carbon molecular sieves have bidisperse pore structures consisting of macropores and micropores, where the gas molecules can diffuse at different time rates.[41] To simplify the mass transfer model, a bilinear driving force (bi-LDF) model was used.[42,43]

As demonstrated in a prior study,[38] it has been established that the ideal gas law remains valid in describing the experimental observation under low-temperature conditions (until 195 K) and pressure up to 18 bar. Darcy's law was used to describe the pressure drop in the column. Accordingly, the mathematical model equations, summarized in Table S4, were implemented in the Aspen Adsorption package, where the method of lines is used to solve the set of coupled partial and algebraic differential equations.[44] The spatial derivatives were discretized by a biased upwind differencing scheme (BUDS) into a uniform grid of 50 points. The boundary conditions for the fixed-bed adsorption model and the VPSA model are summarized in Table S5.

3. RESULTS AND DISCUSSION

3.1. Adsorbent Characterization. The Hg porosimetry results are shown in Figure 3a where it is possible to see a unimodal and narrow macropore size distribution ranging from 211 to 379 nm, which is characteristic of carbon molecular sieves.[45] The CMS-3K-172 textural properties are summarized in Table 1. Figure 3b shows sorption analyses of CO_2 at 273 K, which leads to a micropore surface area equal to 481 $m^2\ g^{-1}$ and a limiting micropore volume equal to 0.19 $cm^3\ g^{-1}$, which compares with values found in the literature.[46−48]

https://doi.org/10.1021/acs.iecr.3c04532
Ind. Eng. Chem. Res. 2024, 63, 6333−6346

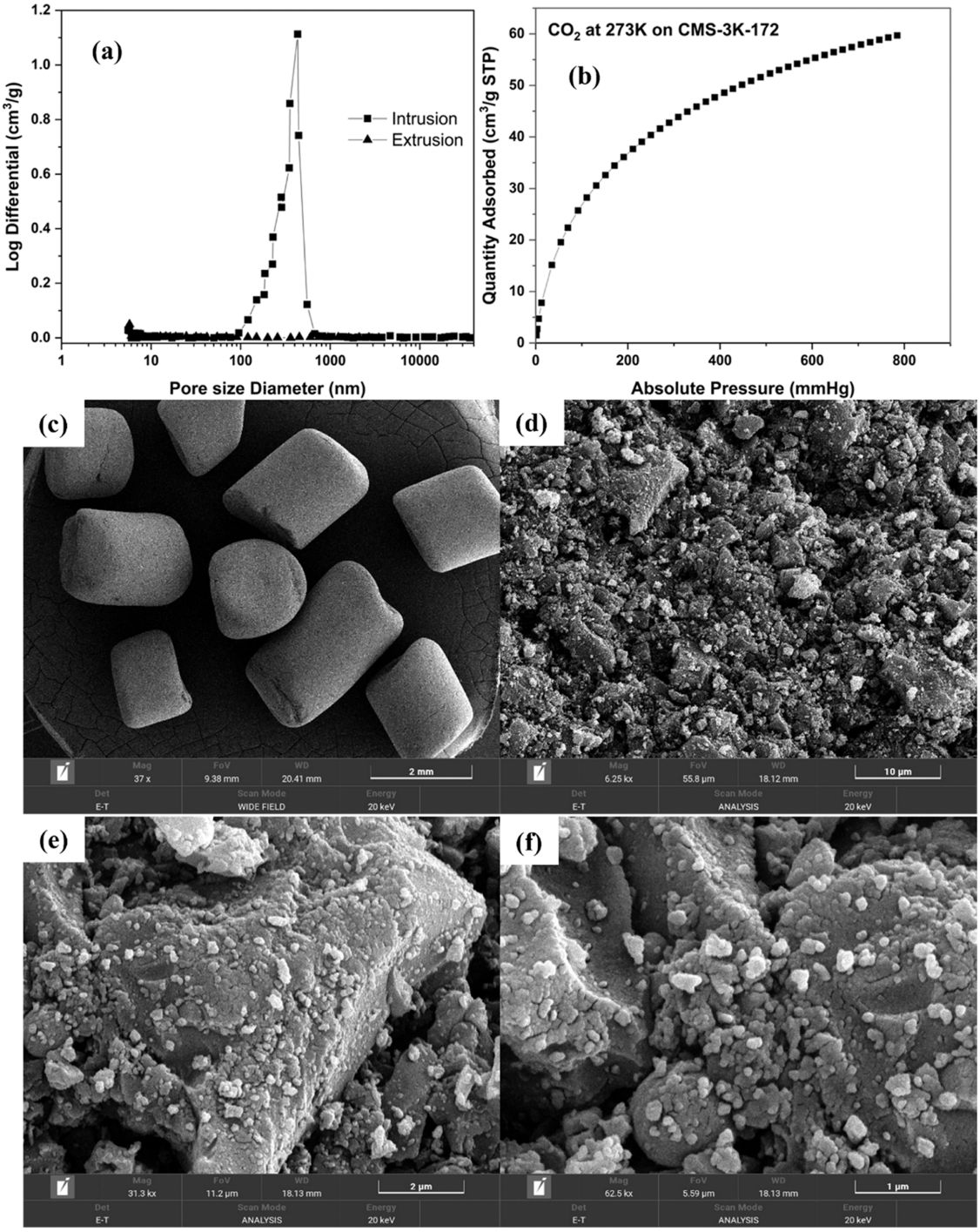

Figure 3. Characterization of CMS-3K-172: (a) differential intrusion and extrusion of Hg in pores; (b) adsorption equilibrium isotherm of CO_2 at 273 K; and (c–f) SEM images.

CMS-3K-172 SEM images are presented in Figure 3c–f, which clearly show that the cylindrical extruded pellets have a defined diameter of around 1.8 mm and lengths ranging between 1.18 and 2.8 mm. Also, Figure 3d–f shows that CMS-3K-172 presents controlled agglomerates or compacts of approximately uniform spheres, which corroborates with the very narrow pore size distribution shown in Figure 3a. From the EDX spectra, placed in Table S6 in the SI, the expected elements were found (C (>97%), Rb, Nb).

3.2. Single-Component Breakthrough Data and Adsorption Isotherms. The H_2 adsorption isotherms in CMS-3K-172 were obtained through a series of breakthrough curve measurements at three temperatures, 195, 231, and 273 K, and pressures of up to 18 bar. The experimental conditions are summarized in Tables S1 and S2 of the SI for CH_4 and H_2, respectively.

Figure 4a–c shows the corresponding observed breakthrough curves for H_2 and CH_4 on CMS-3K-172 and comparison with blank experiments (glass spheres inside the fixed bed). It is possible to see that H_2 is adsorbed on CMS-3K-172 since its breakthrough curve presents a delay compared with the blank experiment. On the opposite, the breakthrough

https://doi.org/10.1021/acs.iecr.3c04532
Ind. Eng. Chem. Res. 2024, 63, 6333−6346

Table 1. Textural Properties of CMS-3K and Fixed-Bed Column Properties

	unit	value
Hg porosity		
total intrusion volume	$cm^3\ g^{-1}$	0.304
total pore area	$m^2\ g^{-1}$	5.760
median pore diameter (volume)	nm	379
median pore diameter (area)	nm	203
average pore diameter ($4V/A$)	nm	211
solid density	$g\ cm^{-3}$	1.495
apparent density	$g\ cm^{-3}$	1.028
porosity	%	31.25
CO_2 adsorption at 273 K		
micropore surface area	$m^2\ g^{-1}$	481
limiting micropore volume	$cm^3\ g^{-1}$	0.193
adsorbent and exp. column properties		
adsorbent shape		cylindrical
adsorbent diameter	mm	1.8
adsorbent length	mm	1.18−2.8
Exp. column porosity		0.4438
Exp. column length	m	0.1
Exp. column diameter	m	0.0046

curves of CH_4 and the blank in the CMS-3K-172 are coincident, which indicates that CH_4 does not enter the pores of CMS-3K-172, in accordance with the literature data.[41−43,49] These results demonstrate that CMS-3K-172 can easily separate H_2 from CH_4. For example, Kowalczyk et al.[48] have shown that the kinetic H_2/CH_4 selectivity, for carbonaceous molecular sieves, is very high, in the order of 10^2−10^3.

All of the single-component breakthrough curves for H_2 on CMS-3K-172 studied in this work are shown in Figure S1 in the SI.

Figure 5 shows the experimental (symbols) and theoretical (lines) isotherms measured for H_2 on CMS-3K-172 from the breakthrough experiments. The maximum loading for H_2 is around 1.38 mol kg^{-1} at 195 K and 12 bar. Moreover, the H_2 isotherm is of type I according to the IUPAC classification,[50] being practically linear. Accordingly, the Langmuir isotherm model fits the experimental data well, as shown in Figure 5. The Langmuir isotherm parameters are summarized in Table 2. The heat of adsorption is around 8.33 kJ mol^{-1}, which is

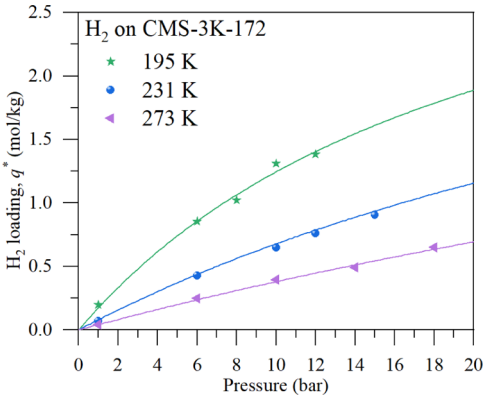

Figure 5. Adsorption equilibrium of H_2 on CMS-3K-172 obtained from breakthrough experiments at 195, 231, and 273 K. Symbols = experimental; solid lines = model.

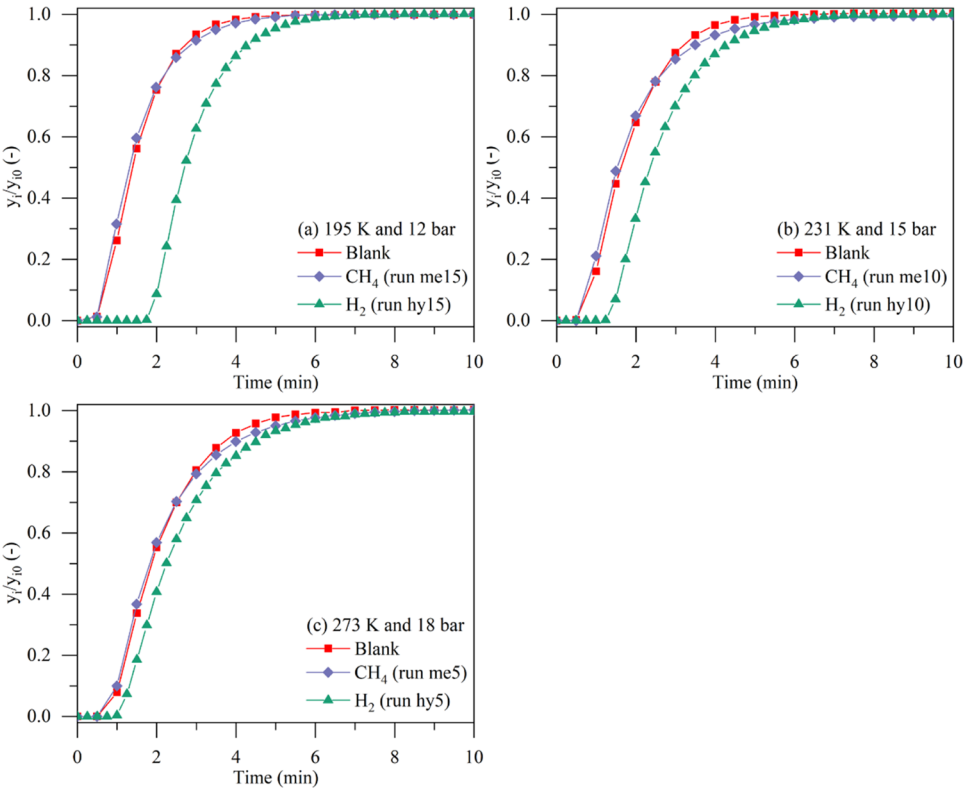

Figure 4. Experimental breakthrough curves of H_2 (green) and CH_4 (purple) on CMS-3K-172 in comparison to the blank experiments (red, column filled with glass sphere) at (a) 195 and 12 bar, (b) 231 and 15 bar, and (c) 273 and 18 bar. The experimental conditions can be found in Tables S1 and S2.

https://doi.org/10.1021/acs.iecr.3c04532
Ind. Eng. Chem. Res. 2024, 63, 6333−6346

Table 2. Langmuir Isotherm Parameters for the Sorption of H_2 on CMS-3K-172

q_m (mol kg^{-1})	b (bar^{-1})	$-\Delta H$ (kJ mol^{-1})	σ^2
3.91	4.67×10^{-2}	8.33	9.0×10^{-5}

very close to the values reported in the literature for H_2 adsorption in similar materials, ranging from 7 to 12 kJ mol^{-1}.[51−54]

3.3. Mathematical Model Validation. The mathematical model was validated through the fitting of binary experimental breakthrough curves, and after that, it was used for the VPSA process simulations. To perform the simulations, the transport parameters were estimated except the H_2 micropore coefficient (k_{mic} = 10 s^{-1}) that was obtained from trial-and-error simulations of the experimental breakthrough curves, as can be observed in Figure S6. For CH_4, the micropore coefficient ($k_{mic} = 1 \times 10^{-4}$ s^{-1}) was taken from Rocha et al.[42] All of the simulation parameters are summarized in Tables S7 and S8 in the SI. Figure 6 shows the binary breakthrough curve for CH_4 and H_2 (80/20 vol %) on CMS-3K-172 and respective fitting, with experimental conditions shown in Table S3 in the SI. The lines in Figure 6 represent model predictions that agree well with the experimental data. The close agreement between experimental and simulated data indicates that the chosen mathematical model conveniently describes the observed fixed-bed dynamic data and can be used to design the VPSA cycle process. It is worth mentioning that since CH_4 takes at least 3 days to reach the equilibrium (in an uptake rate experiment at 308 K) due to its strongly limited diffusion, we consider that it cannot adsorb in CMS-3K-172 in a short VPSA cycle time.[41,43] More details about the mathematical model can be found in the SI (Figure S2 for energy balance considerations and Table S7 for the model parameters).

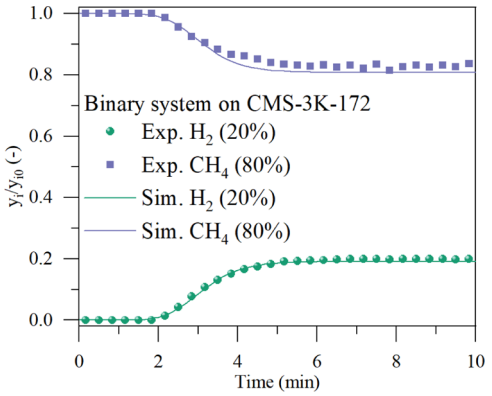

Figure 6. Binary breakthrough curve for a mixture of CH_4/H_2 (80/20 vol %) at 195 K and 12 bar on CMS-3K-172. Symbols = experimental; solid lines = model.

3.4. VPSA Simulations. *3.4.1. Fixed-Bed Dynamics for Base Cycle.* The VPSA base cycle (run 1) comprises 5 steps described in Section 2.5, with the operating conditions summarized in Table 3.

This VPSA configuration corresponds to case (i) shown in Figure 2. A feed mixture of H_2/CH_4 with a ratio of 20/80% was chosen, which is typical of those injected in NGG.[6,30,31] Under the conditions described in Table 3 for run 1, the performance achieved for the final product stream is a recovery of H_2 of 84% with a purity of 65% and the adsorbent productivity of 1748 (mol kg^{-1} day^{-1}). Concerning the dynamics of the VPSA, the cycle steady state (CSS) is achieved in almost 5 cycles, as can be seen in Figure S3 (in the SI), which shows the H_2 axial adsorbed amount profiles along several cycles. Run 1 is simulated in isothermal conditions, and the performance results for nonisothermal (run 1[a]) and adiabatic (run 1[b]) conditions are compared in Table 4. Figure S4 in the SI shows the temperature evolution at the feed/product end, middle, and exhaust end of the column for runs 1[a] and 1[b]. As indicated in Table 4 and Figure S4, temperature effects gave practically the same performance results as those under the isothermal conditions. This is because the heat of adsorption for H_2 is small (ca. 8 kJ mol^{-1}). For example, by comparing run 1 (isothermal) with runs 1[a] (nonisothermal) and 1[b] (adiabatic) in Table 4, the H_2 recovery decreases by 3%, while the H_2 purity increases by 3%. In this way, all of the other simulations described in Table 4 were performed in isothermal conditions.

Table 3. VPSA Process Variables for the Base Cycle with 5 Steps (Run 1)

parameter	value	units	description
t_{PRESS}	10	s	pressurization time
t_{FEED}	5	s	feed time
t_{PURGE}	2	s	H_2 purge time
t_{COD}	5	s	COD time
t_{CVB}	10	s	CVB time
F_{FEED}	97.14	SLPM	feed flow rate
F_{PURGE}	48.57	SLPM	purge flow rate
P_H	30	bar	high pressure
P_I	15	bar	intermediate pressure
P_V	0.1	bar	vacuum pressure
T	195	K	feed temperature
H_2/CH_4	0.2/0.8		molar fraction ratio

The axial profiles of the H_2 molar fraction and adsorbed amount at the end of each step in the CSS for run 1 are shown in Figure 7a,b, respectively. The 5-step VPSA (case(i) in Figure 2) cycle starts with the pressurization step with the feed mixture (H_2/CH_4—20/80%). At the end of the pressurization step, shown in Figure 7a,b (step 1—black line), it can be observed that H_2 spreads through the column due to its low affinity to the adsorbent where the adsorption equilibrium isotherm is not so favorable to self-sharpen the H_2 mass traveling wave. Afterward, the exhaust end is open, and the feed step starts. At the end of the feed step, shown in Figure 7a,b (step 2—red line), the H_2 mass transfer zone (MTZ) is practically spread through almost 50% of the column. In the H_2 purge step, the objective is to purge out the weak adsorptive component by using the strong adsorptive component.[55] Here, pure H_2 is fed at the feed/product end, and Figure 7a,b (step 3—blue line) shows the expected increase of the H_2 partial pressure along the bed resulting into a steeper MTZ.

At the same time, CH_4 present in the void spaces of the adsorbent and bed is purged out through the exhaust end. In the cocurrent depressurization (COD) step, shown in Figure 7a,b (step 4—green line), the feed/product end is closed, and the column is quickly depressurized until an intermediate pressure (15 bar for run 1).

As the pressure decreases, during the COD step, the H_2-adsorbed amount decreases, and consequently, the H_2 molar fraction increases significantly in the gas phase. While the H_2

https://doi.org/10.1021/acs.iecr.3c04532
Ind. Eng. Chem. Res. 2024, 63, 6333−6346

Table 4. Operating Conditions and Process Performance of the VPSA Cycles Simulated for H_2/CH_4 Separation with CMS-3K-172[a]

run	t_{PURGE} (s)	t_{COD} (s)	P/F (−)	P_I/P_H (−)	H_2 recovery (%)	H_2 purity (%)	H_2 productivity (mol kg^{-1} day^{-1})
case (i): 5-step VPSA							
1	2	5	0.5	0.5	84	65	1748
1[a]	2	5	0.5	0.5	81	68	1700
1[b]	2	5	0.5	0.5	81	68	1698
2	2	5	1	0.5	75	79	1549
3	2	5	1.25	0.5	65	85	1351
4	2	5	1.5	0.5	52	89	1059
5	2	5	1.75	0.5	33	91	681
6	2	5	0.5	0.6	88	60	1841
7	2	5	1	0.6	82	75	1708
8	2	5	1.25	0.6	76	80	1577
9	2	5	1.5	0.6	67	85	1373
10	2	5	1.75	0.6	53	88	1090
11	2	5	0.5	0.7	91	56	1904
12	2	5	1	0.7	87	71	1804
13	2	5	1.25	0.7	83	76	1713
14	2	5	1.5	0.7	76	81	1567
15	2	5	1.75	0.7	66	85	1354
case (ii): 4-step VPSA							
16	2		0.25		96	40	2398
17	2		0.5		95	48	2371
18	2		1		93	62	2292
19	2		1.5		86	73	2131
20	5		0.25		95	52	2113
21	5		0.5		92	68	2041
22	5		1		69	89	1514
23	5		1.5		1	96	28
24	8		0.25		88	62	1891
25	8		0.5		85	83	1701
26	8		0.75		53	95	1052
case (iii): 4-step VPSA							
27		5		0.5	87	43	1949
28		5		0.6	91	40	2032
29		5		0.7	93	37	2089
30		10		0.5	88	43	1686
31		10		0.6	91	40	1750
32		10		0.7	94	37	1795

[a][a] Nonisothermal consideration; [b] adiabatic consideration; the other constant parameters are shown in Table 3.

MTZ moves forward to the exhaust end of the column, it displaces CH_4 farther out of the bed. The COD step also helps to increase the H_2 purity in the bed for the next step. In the final countercurrent vacuum blowdown (CVB) step, the exhaust end is closed, and the column is countercurrently depressurized from the intermediate pressure until the vacuum pressure to collect a high purity of H_2 product stream. At the end of the CVB step, it can be observed in Figure 7b (step 5—purple line) that the H_2-adsorbed amount approaches zero (meaning that the bed is cleaned for the next cycle), while the molar fraction (Figure 7a) is around 60% in the feed/product end.

Figure 7c,d shows the total molar flow rate and the component molar fraction histories withdrawn from the column along all of the steps at CSS for run 1, respectively. In steps 2 and 3 (feed and H_2 purge steps, respectively), a CH_4-rich stream (ca. 96%) is obtained in the exhaust end as can be seen in Figure 7d, illustrated by the black dashed line. Even in step 4 (COD step), the molar fraction of CH_4 in the exhaust end is still very high but decreases to around 90%. On the opposite, the molar fraction of H_2 as expected is very high along step 5 (CVB step), starting from a practically pure stream to a constant value of around 60% until the end of the step, where the bed is cleaned from H_2 (adsorbed amount very low) for the next cycle. Also, at the beginning of step 5 (CVB step), the product flow rate increases significantly at the feed/product end due to the evacuation of the column (Figure 7c), but positively this stream is practically pure in H_2 (Figure 7d), which is very important for the overall performance of the VPSA cycle. Along this cycle, the H_2 molar fraction in the product flow rate decreases to around 60% until the bed is practically completely cleaned (Figure 7b). To be noted is also that step 4 (COD step) causes a sudden increase in the total molar flow rate at the exhaust end (Figure 7c), where the H_2 molar fraction slightly increases (Figure 7d), which can negatively impact the H_2 recovery in the final CVB step 5.

3.5. The Effect of Process Variables on VPSA Performance. Here, the parametric study described in Section 2.6 was performed to optimize the VPSA cycle base (run 1) in terms of H_2 purity and recovery. The operating conditions and simulation results are summarized in Table 4, and the column properties and simulation parameters are summarized in Table S8.

3.5.1. Effect of P/F Ratio for Different P_I/P_H Values. The relative importance of the P/F (eq 4) and P_I/P_H (eq 5) ratios in the 5-step VPSA (case (i) in Figure 2) process performance around the base cycle (run 1) were studied and are summarized in Table 4. Figure 8 shows the H_2 recovery and purity as a function of P/F and P_I/P_H ratios from where it is possible to see an opposite trend between H_2 recovery (Figure 8a) and purity (Figure 8b). The higher the P/F, the higher the purity and the lower the recovery. This can be explained since by increasing the P/F ratio, the higher the amount of CH_4 is being displaced out of the column along the H_2 purge step 3, which leads to an increase in the H_2 purity in the final CVB step 5. For instance, by increasing the P/F from 0.5 (run 1) to 1.5 (run 4), the purity increases from 65 to 89% (Table 4). However, the higher the P/F ratio, the higher the amount of H_2 lost in the H_2 purge and COD steps, leading to a lower H_2 recovery. By comparing again runs 1 and 4, the recovery decreases from 84 to 52% as P/F increases from 0.5 to 1.5 (Table 4). The P_I/P_H ratio affects the VPSA performance contrarily compared to the P/F ratio, e.g., the lower the P_I/P_H ratio, the lower the H_2 recovery and the higher the H_2 purity. This effect was observed by comparing runs 1 and 11 in Table 4, e.g., as the P_I/P_H increases from 0.5 to 0.7, the recovery increases from 84 to 91% and the purity decreases from 65 to 56%. Thus, to increase the H_2 molar fraction in the gas phase along the column, and, hence, its purity in the CVB step, the P_I/P_H must be set to the lowest value possible, which agrees with that observed by Chen and Ahn.[56] However, it is worth noting that the lower the P_I/P_H, the lower the H_2 recovery.

The red lines in Figure 8 represent the results for the four-step VPSA without the COD step (case (ii) in Figure 2) and run numbers 17, 18, and 19 in Table 4. The H_2 purge step time was kept with the same values as in the runs with the COD step (runs 1−15). As can be seen, without the COD step, the process achieved the highest recovery (Figure 8a), around 96%, but, on the other hand, these runs were the ones with the lowest purities, between 40 and 73% (Figure 8b). This occurs

https://doi.org/10.1021/acs.iecr.3c04532
Ind. Eng. Chem. Res. 2024, 63, 6333−6346

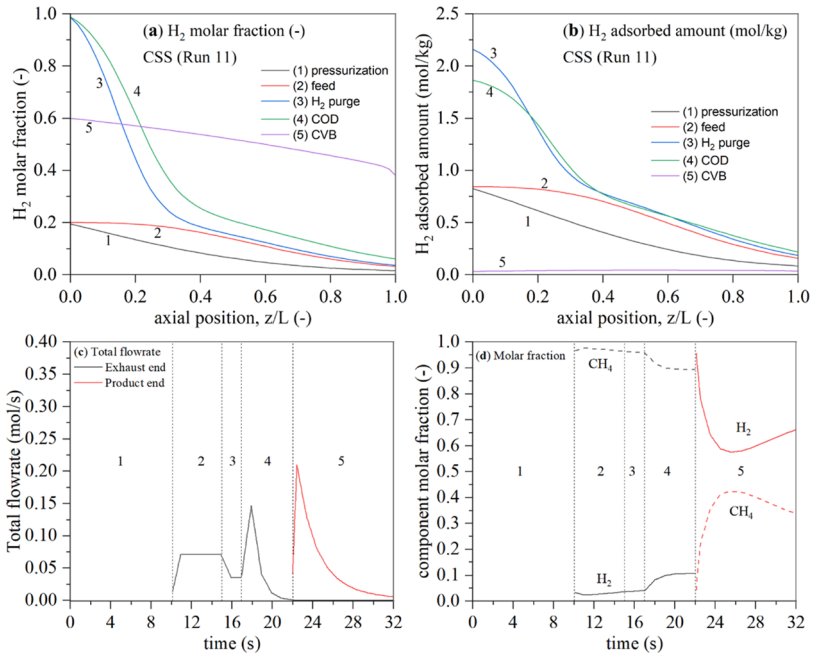

Figure 7. VPSA simulation results for H_2/CH_4 separation with CMS-3K-172 for the 5 cycle steps, shown in Figure 1, in run 1 (base cycle). (a) Axial bed molar fraction of H_2 in the cycle steady state (CSS); (b) axial bed adsorbed amount of H_2 at CSS; (c) total molar flow rate history at the CSS; (d) component molar fraction history at the CSS, CH_4 (dashed lines), and H_2 (solid lines). The numbers shown in the figure represent (1) pressurization, (2) feed, (3) H_2 purge, (4) COD, and (5) CVB steps. On panels (c) and (d), the black lines indicate the history in the exhaust end ($z/L = 1$) and red lines represent the history in the feed/product end ($z/L = 0$). The simulation conditions and performance parameters for run 1 are shown in Tables 3 and 4.

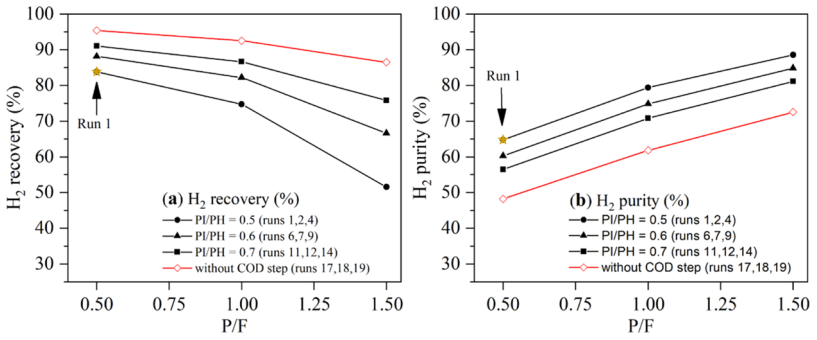

Figure 8. Effects of P/F and P_I/P_H ratios on the (a) H_2 recovery and (b) H_2 purity for the H_2/CH_4 separation by VPSA, using CMS-3K-172.

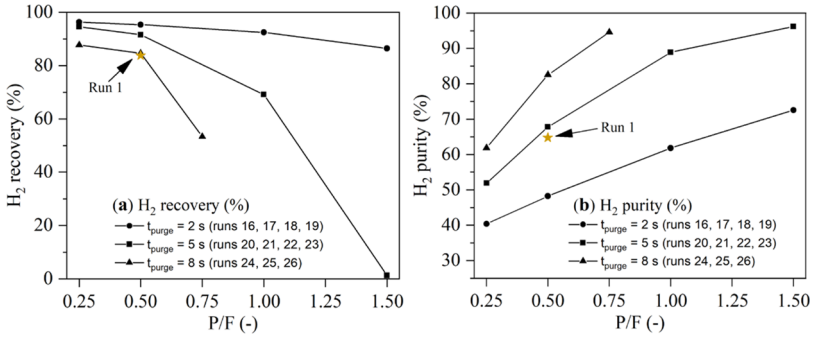

Figure 9. Effects of P/F and H_2 purge step time on the (a) H_2 recovery and (b) H_2 purity for the H_2/CH_4 separation by VPSA, using CMS-3K-172.

because, during the H_2 purge step, the H_2 partial pressure inside the column becomes higher, which leads to a steeper MTZ moving faster in the bed. Consequently, the H_2 wavefront displaces a larger amount of CH_4 in the bed through the exhaust end before the CVB step (i.e., and without too much H_2 spent at the exhaust end). Thus, at the end of the H_2 purge step, a great part of H_2 molecules in the gas and solid phases remain inside the column, being recovered during the following CVB step, which explains the highest recovery of H_2 achieved for the 4-step VPSA (case (ii)) in comparison with

https://doi.org/10.1021/acs.iecr.3c04532
Ind. Eng. Chem. Res. 2024, 63, 6333−6346

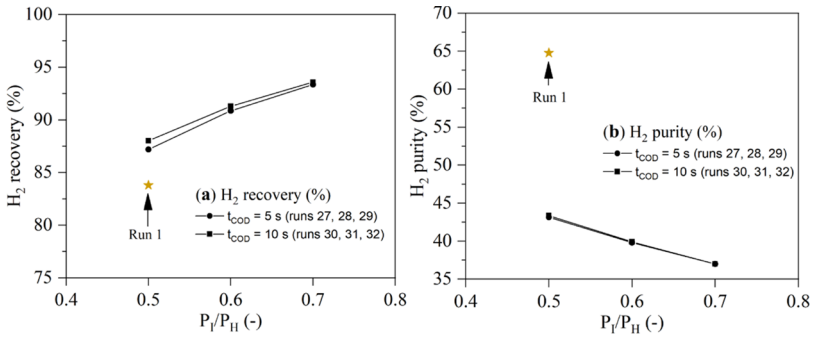

Figure 10. Effects of P_I/P_H and COD step time on the (a) H_2 recovery and (b) H_2 purity for the H_2/CH_4 separation by VPSA (without H_2 purge step), using CMS-3K-172.

the 5-step VPSA (case (i)). To increase the H_2 purity in the final CVB step, the H_2 purge step can be extended in time as discussed in the next section. Looking at Figure 7d, we can see that during the COD step, in the base cycle (run 1), some H_2 is spent at the exhaust end, which explains the overall lowest recovery using a 5-step VPSA (case (i)). The COD step can be advantageous when it does not result in significant losses of the more adsorptive component.

3.5.2. Effect of P/F Ratio for Different H_2 Purge Step Time Values. Steps 3 and 4 (H_2 purge and COD steps, respectively) are used with the same purpose, reduce the partial pressure of CH_4 in the gas phase in both adsorbent and column voids before the final CVB step, to increase the final product H_2 purity and recovery. The effect of each step in the VPSA was studied separately through cases ii and (iii). In this study, the COD step was removed from the VPSA (case (ii) in Figure 2), and only the H_2 purge step was used to reduce the CH_4 partial pressure inside the column. Figure 9 shows the relative importance of the H_2 purge step time for different P/F ratios in the H_2 recovery and purity. As shown in Figure 9a, as the H_2 purge time increases, from 2 to 8 s, the recovery decreases, e.g., from 93 to 69% (runs 18 and 22, respectively). Figure 9b shows the opposite trend for the purity, as the higher the H_2 purge time, the higher the H_2 purity, e.g., from 62 to 89% (runs 18 and 22, respectively). This occurs because the higher the H_2 purge step time, the higher the amount of CH_4 that will be taken out of the column before the following CVB step. For instance, for P/F equal to 0.5, H_2 purity increases from 48 to 83% by increasing the H_2 purge time from 2 to 8 s. However, there is a limiting H_2 purge time that can be used to maximize the purity without significantly decreasing the H_2 recovery. For a constant H_2 purge time, the effects of the P/F ratio in the H_2 recovery and purity shown in Figure 9 are similar to those observed in Figure 8. The performance parameters for run 1 are also represented in Figure 9a,b, which can be seen that for the 4-step VPSA (without COD, case (ii)) several combinations can provide better performance parameters than for run 1. For example, H_2 purity up to 68% with a recovery of 92% is achieved by using case (ii) 4-step VPSA in run 21, as shown in Table 4 and Figure 9.

3.5.3. Effect of P_I/P_H Ratio for Different COD Step Time Values. In this parametric study, only the COD step was used to reduce the CH_4 partial pressure inside the column before the CVB step. This is the 4-step VPSA configuration case (iii) presented in Figure 2. In this way, the relative importance of P_I/P_H ratio and COD step times in the VPSA performance are illustrated in Figure 10. The H_2 recovery increases with increasing values of P_I/P_H (Figure 10a), while the H_2 purity decreases (Figure 10b). For example, as the P_I/P_H increases from 0.5 to 0.7, the recovery increases from 87 to 93% and the purity decreases from 43 to 37% (runs 27 and 29, respectively). Interestingly, the H_2 recovery and purity seem not to be affected by the COD time as indicated in Figure 10 since they are almost the same by using 5 or 10 s of the COD time for a fixed P_I/P_H, a result also observed elsewhere.[57] In this way, only the ratio P_I/P_H has a major influence on the performance of the overall cycle with the COD step. Accordingly, as P_I becomes close to P_H, i.e., for high values of the P_I/P_H ratio, lower is the molar flow rate that leaves the column, and, consequently, lower the H_2 purity and higher the H_2 recovery as depicted in Figure 10. From Table 4, the 4-step VPSA (case (iii) without the H_2 purge step) can concentrate H_2 up to 43% only with a recovery of 87% (run 27) and adsorbent productivity equal to 1949 mol kg^{-1} day^{-1}, indicating lower performance compared with the 5-step VPSA (case (i)) and 4-step VPSA (case (ii)). For a comparison, Figure 10 also shows the performance parameters for run 1 (5-step VPSA (case (i)), where the 4-step VPSA (case (iii)) provides lower H_2 purity values).

3.5.4. Effect of the VPSA Configuration Cases. Three VPSA cases were studied, namely, case (i): a 5-step VPSA described in Section 2.5, case (ii): a 4-step VPSA without COD step 4, and case (iii): a 4-step VPSA without H_2 purge step 3, as shown in Figure 2.

In case (i) 5-step VPSA, as mentioned before, the H_2 purge (step 3) and COD (step 4) steps work with the same purpose, reduce the partial pressure of CH_4 in the gas phase for both the adsorbent and column voids to maximize the H_2 purity and recovery during the final CVB step. During the H_2 purge step 3, Figure 7a, there are two regions in the bed, a zone filled with pure H_2 near the feed/product end to almost 30% of bed length and another with a similar composition of the feed mixture at almost 60% of the bed. As the H_2 pressure increases, the isotherm becomes more favorable, MTZ being steeper near the feed end. This is important to displace CH_4 from the bed without losing too much H_2 at the exhaust end of the column (Figure 7d, step 3). Consequently, in the following COD step, the steeper high-purity H_2 MTZ moves faster in the bed in the direction of the exhaust end resulting in an increasing spent of H_2 and consequently decreasing H_2 recovery in the overall process (Figure 7d). For example, Table 4 shows that run 5, which has higher P/F and lower P_I/P_H ratios, leads to a higher displacement of CH_4 throughout the column at the exhaust end and, consequently, we can obtain a high purity of 91%. However, some H_2 is lost together with CH_4 in the COD step resulting in a lower H_2 recovery of only 33% for run 5. Thus,

https://doi.org/10.1021/acs.iecr.3c04532
Ind. Eng. Chem. Res. 2024, 63, 6333−6346

the COD step needs to be short and the P_I/P_H needs to be high to avoid a significant loss of H_2 in purge step 3 and COD step 4 at the exhaust end.

To reduce the H_2 lost in steps 3 and 4, the COD step was removed before the CVB step (step 5). This is a VPSA configuration with a 4-step case (ii). In this way, we can decrease the loss of H_2 through the exhaust end of the column, leading to an improvement in the H_2 recovery and purity during the final CVB step. Accordingly, the performance values for case (ii) 4-step VPSA (run 21) are 92% recovery with 68% purity (Table 4), which leads to an increase of 21% in the H_2 purity as compared with run 11 (5-step VPSA).

Another 4-step configuration was considered to improve H_2 purity and recovery by keeping the COD step (step 4) and removing the H_2 purge step (step 3). This is the so-called 4-step VPSA-case (iii), where after the feed step, only the COD step (step 4) preceded the CVB step (step 5). In this case, it lost the effect of concentrating H_2 before the final CVB step. Thus, the VPSA configuration leads to performance with high H_2 recoveries but with lower purities, as can be seen in Table 4 for runs 27−32. Moreover, by using only the COD step before the CVB step, the H_2 recovery and purity decrease around 4 and 23%, respectively, when comparing run 11 (5-step VPSA) with run 27 (4-step VPSA) in Table 4.

3.5.5. Effect of the H_2 Initial Concentration. The H_2 initial concentration was varied from 20 to 50% in the same cycle conditions of runs 16−19 (case (ii) 4-step VPSA), which showed the best results in Table 4 in terms of H_2 recovery. This range was considered because the effect of adding up to 50% of H_2 into the NGG is under commercial consideration.[34] Figure 11 shows the H_2 recovery and purity for different H_2 feed value concentrations. As can be seen, as higher the H_2 feed concentration, the higher the H_2 purity and lower the H_2 recovery. For instance, comparing run 16 with H_2 feed concentrations of 20% (black square) and 50% (blue triangle), the recovery decreases from 96 to 89% and the purity increases from 40 to 70%. This is expected since as the H_2 concentration in the feed increases, the contamination with CH_4 along the bed is lower before the CVB step, improving the final product H_2 purity. On the other hand, as the concentration of H_2 is higher in steps 1 and 2, the respective concentration front moves faster through the axial position of the bed (favorable isotherm), increasing the losses in the exhaust end and thus reducing the H_2 recovery. This is seen in Figure S5 of the SI that illustrates the H_2 molar fraction profile in the bed at the end of the feed step for run 16 for different H_2 feed concentrations. Overall, the increasing H_2 feed concentration in this newly proposed conceptual VPSA cycle results in a better overall process performance, especially the level of purity of the final H_2 product stream collected in the CVB step.

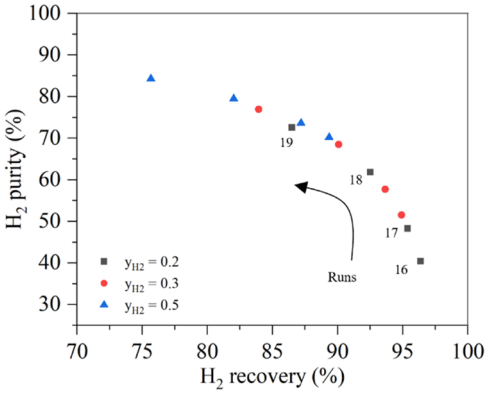

Figure 11. Effect of the H_2 initial concentration on the purity and recovery of case (ii) 4-step VPSA. Simulation conditions for runs 16−19 are shown in Table 4.

4. CONCLUSIONS

In this study, the recovery of GH from NGG using a new conceptual VPSA cycle was evaluated. The separation of H_2 from CH_4 was achieved by employing the CMS-3K-172 adsorbent, which exhibits a moderate adsorption capacity for H_2 and kinetically separates it from CH_4. The H_2 adsorption equilibrium was studied between 195 and 273 K and conveniently fitted with a Langmuir isotherm. Furthermore, a mathematical model, developed in Aspen Adsorption, was validated by fitting binary fixed-bed breakthrough curves for further simulations of three different VPSA process configurations with 5 and 4 steps. The 4-step VPSA (case (ii)), without the COD step, allows obtaining a H_2 purity of up to 68% with a recovery of up to 92%, being the best trade-off between purity and recovery achieved with 83% purity and 85% recovery. This 4-step VPSA (case (ii)) showed better performance as compared to the 5-step VPSA (case (i)) and 4-step VPSA (case (iii)) because the H_2 purge step has a positive effect in preventing the losses of H_2 through the exhaust end of the column, leading to an improvement of the H_2 recovery (up to 96%) with high purity (up to 89%) during the following final CVB step. On the contrary, the 4-step VPSA (case (iii)) with only the COD step does not improve the VPSA process because the amount of CH_4 remaining inside the column before the final CVB is still very high, which severely impacts the H_2 purity. In summary, as interest and demand for green hydrogen continue to increase, the conceptual VPSA proposed in this study exhibits great potential for the recovery of green hydrogen from natural gas grids. The VPSA allows for the effective concentration of H_2 from 20 to 68%, with recovery of up to 92%. This VPSA process can be used as a pre-enrichment step, which subsequently can be directly followed into an already commercial conventional PSA processes that utilizes adsorbents with a strong equilibrium affinity for CH_4 (e.g., with zeolites 5A or 13 X) to produce H_2 from NGG with a higher purity level (>99.97%).

■ ASSOCIATED CONTENT

Supporting Information

The Supporting Information is available free of charge at https://pubs.acs.org/doi/10.1021/acs.iecr.3c04532.

Additional experimental details, material characterization, and mathematical model details, including figures of tables (PDF)

■ AUTHOR INFORMATION

Corresponding Authors

Lucas F. A. S. Zafanelli − *Centro de Investigação de Montanha (CIMO), Instituto Politécnico de Bragança, 5300-253 Bragança, Portugal; Laboratório Associado para a Sustentabilidade e Tecnologia em Regiões de Montanha (SusTEC), Instituto Politécnico de Bragança, 5300-253 Bragança, Portugal; LSRE-LCM—Laboratory of Separation and Reaction Engineering-Laboratory of Catalysis and Materials, Faculty of Engineering, University of Porto, 4200-*

https://doi.org/10.1021/acs.iecr.3c04532
Ind. Eng. Chem. Res. 2024, 63, 6333−6346

465 Porto, Portugal; ALiCE—Associate Laboratory in Chemical Engineering, Faculty of Engineering, University of Porto, 4200-465 Porto, Portugal; orcid.org/0000-0001-5187-2042; Email: zafanelli@ipb.pt

José A. C. Silva − *Centro de Investigação de Montanha (CIMO), Instituto Politécnico de Bragança, 5300-253 Bragança, Portugal; Laboratório Associado para a Sustentabilidade e Tecnologia em Regiões de Montanha (SusTEC), Instituto Politécnico de Bragança, 5300-253 Bragança, Portugal;* orcid.org/0000-0003-1778-3833; Email: jsilva@ipb.pt

Authors

Ezzeldin Aly − *Centro de Investigação de Montanha (CIMO), Instituto Politécnico de Bragança, 5300-253 Bragança, Portugal; Laboratório Associado para a Sustentabilidade e Tecnologia em Regiões de Montanha (SusTEC), Instituto Politécnico de Bragança, 5300-253 Bragança, Portugal;* orcid.org/0000-0003-4840-2597

Adriano Henrique − *Centro de Investigação de Montanha (CIMO), Instituto Politécnico de Bragança, 5300-253 Bragança, Portugal; Laboratório Associado para a Sustentabilidade e Tecnologia em Regiões de Montanha (SusTEC), Instituto Politécnico de Bragança, 5300-253 Bragança, Portugal;* orcid.org/0000-0002-5227-9790

Alírio E. Rodrigues − *LSRE-LCM—Laboratory of Separation and Reaction Engineering-Laboratory of Catalysis and Materials, Faculty of Engineering, University of Porto, 4200-465 Porto, Portugal; ALiCE—Associate Laboratory in Chemical Engineering, Faculty of Engineering, University of Porto, 4200-465 Porto, Portugal;* orcid.org/0000-0002-0715-4761

Georges Mouchaham − *Institut des Matériaux Poreux de Paris, Ecole Normale Supérieure de Paris, ESPCI Paris, CNRS, PSL University, 75005 Paris, France;* orcid.org/0000-0001-8696-9733

Complete contact information is available at: https://pubs.acs.org/10.1021/acs.iecr.3c04532

Notes

The authors declare no competing financial interest.

■ ACKNOWLEDGMENTS

The authors are grateful to the Foundation for Science and Technology (FCT, Portugal) for financial support: (1) under project PTDC/EQU-EPQ/0467/2020 (DOI: 10.54499/PTDC/EQU-EPQ/0467/2020), (2) through the national funds FCT/MCTES (PIDDAC), CIMO UIDB/00690/2020 (DOI: 10.54499/UIDB/00690/2020) and UIDP/00690/2020 (DOI: 10.54499/UIDP/00690/2020); and SusTEC, LA/P/0007/2020 (DOI: 10.54499/LA/P/0007/2020), (3) by the national funds through FCT/MCTES (PIDDAC): LSRE-LCM, UIDB/50020/2020 (DOI: 10.54499/UIDB/50020/2020) and UIDP/50020/2020 (DOI: 10.54499/UIDP/50020/2020), and ALiCE, LA/P/0045/2020 (DOI: 10.54499/LA/P/0045/2020). Additionally, the authors thank the national funding by FCT, Foundation for Science and Technology, through the individual research grant SFRH/BD/7925/2020 of L.F.A.S.Z. Moreover, the authors are grateful to Osaka Co. for kindly providing the CMS-3K-172 studied in this work.

■ NOMENCLATURE

a_p	specific area of the pellet (m^{-1})
a_c	specific area of the column (m^{-1})
b_i	adsorption equilibrium constant of component i (bar^{-1})
$b_{\infty,i}$	pre-exponential factor of the affinity constant at an infinite temperature of component i (bar^{-1})
C	total gas concentration (mol m^{-3})
C_f	feed gas concentration (mol m^{-3})
C_{pg}	heat capacity of gas (J mol^{-1} K^{-1})
C_{ps}	adsorbent specific heat capacity (J mol^{-1} K^{-1})
d_b	bead diameter (m)
d_c	column diameter (m)
D_{ax}	axial mass dispersion coefficient (m^2 s^{-1})
D_m	molecular diffusivity (m^2 s^{-1})
D_p	macropore diffusion coefficient (m^2 s^{-1})
D_c	micropore diffusion coefficient (m^2 s^{-1})
F	total molar flow rate (mol s^{-1})
h_w	constant heat transfer between gas and wall (W m^{-2} K^{-1})
h_p	film heat transfer coefficient (W m^{-2} K^{-1})
k_{mic}	micropore constant coefficient (s^{-1})
k_{mac}	macropore constant coefficient (s^{-1})
K_p	Darcy's law coefficient (-)
K_{ax}	effective axial bed thermal conductivity (W m^{-1} K^{-1})
K_s	adsorbent thermal conductivity (W m^{-1} K^{-1})
L_c	length of the column (m)
M_i	molecular mass of component i (kg $kmol^{-1}$)
m_{ads}	mass of the adsorbent (kg)
p_i	partial pressure of component i (bar)
P	total pressure of the column (bar)
$\overline{q}_i$	average adsorbed phase concentration of component i (mol kg^{-1})
q^*	equilibrium adsorbed concentration of the component (mol kg^{-1})
q_m	maximum adsorbed phase concentration (mol kg^{-1})
R	universal gas constant (J mol^{-1} K^{-1})
R_p	adsorbent particle radius (m)
r_c	crystal radius (m)
t	time (s)
v_i	interstitial velocity (m s^{-1})
$v_g = v_i\varepsilon_b$	superficial velocity (m s^{-1})
y_i	molar fraction of component i (-)
z	axial coordinate in the bed (m)

■ GREEK LETTERS

ΔH_i	heat adsorption of species i (J mol^{-1})
ΔH_{st}	isosteric heat adsorption (J mol^{-1})
ε_b	bed porosity
ε_p	particle porosity
ρ_p	solid density (kg m^{-3})
ρ_s	apparent adsorbent density (kg m^{-3})
ρ_b	bulk density (kg m^{-3})

■ REFERENCES

(1) Abe, J. O.; Popoola, A. P. I.; Ajenifuja, E.; Popoola, O. M. Hydrogen energy, economy and storage: Review and recommendation. *Int. J. Hydrogen Energy* **2019**, *44* (29), 15072−15086.

(2) IRENA. *Decarbonising End-Use Sectors: Green Hydrogen Certification*; International Renewable Energy Agency, 2022.

(3) Dehdari, L.; Burgers, I.; Xiao, P.; Li, K. G.; Singh, R.; Webley, P. A. Purification of hydrogen from natural gas/hydrogen pipeline mixtures. *Sep. Purif. Technol.* **2022**, *282*, No. 120094.

(4) Atilhan, S.; Park, S.; El-Halwagi, M. M.; Atilhan, M.; Moore, M.; Nielsen, R. B. Green hydrogen as an alternative fuel for the shipping industry. *Curr. Opin. Chem. Eng.* **2021**, *31*, No. 100668.
(5) Melaina, M. W.; Antonia, O.; Penev, M. *Blending Hydrogen into Natural Gas Pipeline Networks: A Review of Key Issues*, 2013.
(6) Liemberger, W.; Gross, M.; Miltner, M.; Prazak-Reisinger, H.; Harasek, M. Extraction of Green Hydrogen at Fuel Cell Quality from Mixtures with Natural Gas. *Chem. Eng. Trans.* **2016**, *52*, 427−432.
(7) Liemberger, W.; Halmschlager, D.; Miltner, M.; Harasek, M. Efficient extraction of hydrogen transported as co-stream in the natural gas grid - The importance of process design. *Appl. Energy* **2019**, *233*−*234*, 747−763.
(8) Aly, E.; Zafanelli, L. F. A. S.; Henrique, A.; Pires, M. G.; Rodrigues, A. E.; Gleichmann, K.; Silva, J. A. C. Fixed Bed Adsorption of CO_2, CH_4, and N_2 and Their Mixtures in Potassium-Exchanged Binder-Free Beads of Y Zeolite. *Ind. Eng. Chem. Res.* **2021**, *60* (42), 15236−15247.
(9) Zafanelli, L. F. A. S.; Henrique, A.; Karimi, M.; Rodrigues, A. E.; Silva, J. A. C. Single- and Multicomponent Fixed Bed Adsorption of CO_2, CH_4, and N_2 in Binder-Free Beads of 4A Zeolite. *Ind. Eng. Chem. Res.* **2020**, *59* (30), 13724−13734.
(10) Zafanelli, L. F. A. S.; Henrique, A.; Steldinger, H.; de Tuesta, J. L. D.; Glasel, J.; Rodrigues, A. E.; Gomes, H. T.; Etzold, B. J. M.; Silva, J. A. C. 3D-printed activated carbon for post-combustion CO_2 capture. *Microporous Mesoporous Mater.* **2022**, *335*, No. 111818.
(11) Plaza, M. G.; García, S.; Rubiera, F.; Pis, J. J.; Pevida, C. Post-combustion CO_2 capture with a commercial activated carbon: Comparison of different regeneration strategies. *Chem. Eng. J.* **2010**, *163* (1−2), 41−47.
(12) Plaza, M. G.; Martínez, S.; Rubiera, F. CO_2 capture, use, and storage in the cement industry: State of the art and expectations. *Energies* **2020**, *13* (21), 5692.
(13) Rajagopalan, A. K.; Rajendran, A. The effect of nitrogen adsorption on vacuum swing adsorption based post-combustion CO_2 capture. *Int. J. Greenhouse Gas Control* **2018**, *78*, 437−447.
(14) Shen, C.; Yu, J.; Li, P.; Grande, C. A.; Rodrigues, A. E. Capture of CO_2 from flue gas by vacuum pressure swing adsorption using activated carbon beads. *Adsorption* **2011**, *17* (1), 179−188.
(15) Agueda, V. I.; Delgado, J. A.; Uguina, M. A.; Brea, P.; Spjelkavik, A. I.; Blom, R.; Grande, C. Adsorption and diffusion of H_2, N_2, CO, CH_4 and CO_2 in UTSA-16 metal-organic framework extrudates. *Chem. Eng. Sci.* **2015**, *124*, 159−169.
(16) Brea, P.; Delgado, J. A.; Águeda, V. I.; Gutiérrez, P.; Uguina, M. A. Multicomponent adsorption of H_2, CH_4, CO and CO_2 in zeolites NaX, CaX and MgX. Evaluation of performance in PSA cycles for hydrogen purification. *Microporous Mesoporous Mater.* **2019**, *286*, 187−198.
(17) Grande, C. A.; Blom, R.; Andreassen, K. A.; Stensrød, R. E. *Experimental Results of Pressure Swing Adsorption (PSA) for Pre-combustion CO_2 Capture with Metal Organic Frameworks*; Dixon, T.; Laloui, L.; Twinning, S., Eds.; Elsevier Ltd., 2017; Vol. *114*, pp 2265−2270.
(18) Chai, S. W.; Kothare, M. V.; Sircar, S. Rapid pressure swing adsorption for reduction of bed size factor of a medical oxygen concentrator. *Ind. Eng. Chem. Res.* **2011**, *50* (14), 8703−8710.
(19) Rao, V. R.; Farooq, S.; Krantz, W. B. Design of a two-step pulsed pressure-swing adsorption-based oxygen concentrator. *AIChE J.* **2010**, *56* (2), 354−370.
(20) Rao, V. R.; Kothare, M. V.; Sircar, S. Novel design and performance of a medical oxygen concentrator using a rapid pressure swing adsorption concept. *AIChE J.* **2014**, *60* (9), 3330−3335.
(21) Wu, C. W.; Vemula, R. R.; Kothare, M. V.; Sircar, S. Experimental Study of a Novel Rapid Pressure-Swing Adsorption Based Medical Oxygen Concentrator: Effect of the Adsorbent Selectivity of N_2 over O_2. *Ind. Eng. Chem. Res.* **2016**, *55* (16), 4676−4681.
(22) Grande, C. A.; Morence, D. G. B.; Bouzga, A. M.; Andreassen, K. A. Silica Gel as a Selective Adsorbent for Biogas Drying and Upgrading. *Ind. Eng. Chem. Res.* **2020**, *59* (21), 10142−10149.
(23) Hosseini, S. S.; Denayer, J. F. M. Biogas upgrading by adsorption processes: Mathematical modeling, simulation and optimization approach - A review. *J. Environ. Chem. Eng.* **2022**, *10* (3), No. 107483.
(24) Martins, J. A.; Miguel, C. V.; Rodrigues, A. E.; Madeira, L. M. Novel Adsorption-Reaction Process for Biomethane Purification/Production and Renewable Energy Storage. *ACS Sustainable Chem. Eng.* **2022**, *10* (24), 7833−7851.
(25) Verougstraete, B.; Schoukens, M.; Sutens, B.; Vanden Haute, N.; De Vos, Y.; Rombouts, M.; Denayer, J. F. M. Electrical swing adsorption on 3D-printed activated carbon monoliths for CO_2 capture from biogas. *Sep. Purif. Technol.* **2022**, *299*, No. 121660.
(26) Brântuas, P. F.; Henrique, A.; Wahiduzzaman, M.; von Wedelstedt, A.; Maity, T.; Rodrigues, A. E.; Nouar, F.; Lee, U. H.; Cho, K. H.; Maurin, G.; et al. Separation of Branched Alkanes Feeds by a Synergistic Action of Zeolite and Metal-Organic Framework. *Adv. Sci.* **2022**, *9* (22), No. 2201494.
(27) Henrique, A.; Maity, T.; Zhao, H.; Brântuas, P. F.; Rodrigues, A. E.; Nouar, F.; Ghoufi, A.; Maurin, G.; Silva, J. A. C.; Serre, C. Hexane isomers separation on an isoreticular series of microporous Zr carboxylate metal organic frameworks. *J. Mater. Chem. A* **2020**, *8* (34), 17780−17789.
(28) Henrique, A.; Rodrigues, A. E.; Silva, J. A. C. Fixed bed dynamics of single and multicomponent adsorption of pentane and hexane isomers in ZIF-8. *Sep. Purif Technol.* **2020**, *238*, No. 116419.
(29) Bárcia, P. S.; Silva, J. A. C.; Rodrigues, A. E. Octane Upgrading of C_5/C_6 Light Naphtha by Layered Pressure Swing Adsorption. *Energy Fuels* **2010**, *24* (9), 5116−5130.
(30) Ogden, J.; Jaffe, A. M.; Scheitrum, D.; McDonald, Z.; Miller, M. Natural gas as a bridge to hydrogen transportation fuel: Insights from the literature. *Energy Policy* **2018**, *115*, 317−329.
(31) Pellegrino, S.; Lanzini, A.; Leone, P. Greening the gas network − The need for modelling the distributed injection of alternative fuels. *Renewable Sustainable Energy Rev.* **2017**, *70*, 266−286.
(32) Burgers, I.; Dehdari, L.; Xiao, P.; Li, K. G.; Goetheer, E.; Webley, P. Techno-economic analysis of PSA separation for hydrogen/natural gas mixtures at hydrogen refuelling stations. *Int. J. Hydrogen Energy* **2022**, *47* (85), 36163−36174.
(33) Dehdari, L.; Amani, M. J.; Parsaei, R. Prediction of water solubility in ill-defined hydrocarbons at high temperatures: Modeling with the CPA-EoS. *Fluid Phase Equilib.* **2017**, *454*, 11−21.
(34) Dehdari, L.; Xiao, P. Y.; Li, K. G.; Singh, R.; Webley, P. A. Separation of hydrogen from methane by vacuum swing adsorption. *Chem. Eng. J.* **2022**, *450*, No. 137911.
(35) Liemberger, W.; Gross, M.; Miltner, M.; Harasek, M. Experimental analysis of membrane and pressure swing adsorption (PSA) for the hydrogen separation from natural gas. *J. Cleaner Prod.* **2017**, *167*, 896−907.
(36) Liemberger, W.; Miltner, M.; Harasek, M. Reduced Model Describing Efficient Extraction of Hydrogen Transported as Co-Stream in the Natural Gas Grid. *Comput.-Aided Chem. Eng.* **2018**, *43*, 1383−1388.
(37) Gleichmann, K.; Unger, B.; Brandt, A. *Industrial Zeolite Molecular Sieves*; IntechOpen, 2016.
(38) Zafanelli, L. F. A. S.; Aly, E.; Rodrigues, A. E.; Silva, J. A. C. A novel cryogenic fixed-bed adsorption apparatus for studying green hydrogen recovery from natural gas grids. *Sep. Purif. Technol.* **2023**, *307*, No. 122824.
(39) Cen, P. L.; Yang, R. T. Separation of Binary Gas-Mixture into 2 High-Purity Products by a New Pressure Swing Adsorption Cycle. *Sep. Sci. Technol.* **1986**, *21* (9), 845−864.
(40) Yang, R. T. Pressure-Swing Adsorption: Principles and Processes. In *Gas Separation by Adsorption Processes*; Yang, R. T., Ed.; Butterworth-Heinemann, 1987; Chapter 7, pp 237−274.
(41) Cavenati, S.; Grande, C. A.; Rodrigues, A. E. Separation of methane and nitrogen by adsorption on carbon molecular sieve. *Sep. Sci. Technol.* **2005**, *40* (13), 2721−2743.

https://doi.org/10.1021/acs.iecr.3c04532
Ind. Eng. Chem. Res. 2024, 63, 6333−6346

(42) Rocha, L. A. M.; Andreassen, K. A.; Grande, C. A. Separation of CO_2/CH_4 using carbon molecular sieve (CMS) at low and high pressure. *Chem. Eng. Sci.* **2017**, *164*, 148−157.
(43) Grande, C. A.; Rodrigues, A. E. Biogas to fuel by vacuum pressure swing adsorption - I. Behavior of equilibrium and kinetic-based adsorbents. *Ind. Eng. Chem. Res.* **2007**, *46* (13), 4595−4605.
(44) Schiesser, W. E.; Griffiths, G. W. *A Compendium of Partial Differential Equation Models: Method of Lines Analysis with Matlab*; Cambridge University Press, 2009.
(45) Lemcoff, N. O. Nitrogen Separation from Air by Pressure Swing Adsorption. In *Studies in Surface Science and Catalysis*; Dąbrowski, A., Ed.; Elsevier, 1999; Vol. *120*, pp 347−370.
(46) Arami-Niya, A.; Rufford, T. E.; Birkett, G.; Zhu, Z. Gravimetric adsorption measurements of helium on natural clinoptilolite and synthetic molecular sieves at pressures up to 3500 kPa. *Microporous Mesoporous Mater.* **2017**, *244*, 218−225.
(47) Zhao, X.; Villar-Rodil, S.; Fletcher, A. J.; Thomas, K. M. Kinetic Isotope Effect for H2 and D2 Quantum Molecular Sieving in Adsorption/Desorption on Porous Carbon Materials. *J. Phys. Chem. B* **2006**, *110* (20), 9947−9955.
(48) Kowalczyk, P.; Gauden, P. A.; Terzyk, A. P.; Furmaniak, S. Microscopic model of carbonaceous nanoporous molecular sieves—anomalous transport in molecularly confined spaces. *Phys. Chem. Chem. Phys.* **2010**, *12* (37), 11351−11361.
(49) Grande, C. A.; Cavenati, S.; Da Silva, F. A.; Rodrigues, A. E. Carbon molecular sieves for hydrocarbon separations by adsorption. *Ind. Eng. Chem. Res.* **2005**, *44* (18), 7218−7227.
(50) Thommes, M.; Kaneko, K.; Neimark, A. V.; Olivier, J. P.; Rodriguez-Reinoso, F.; Rouquerol, J.; Sing, K. S. W. Physisorption of gases, with special reference to the evaluation of surface area and pore size distribution (IUPAC Technical Report). *Pure Appl. Chem.* **2015**, *87* (9−10), 1051−1069.
(51) Jee, J.-G.; Kim, M.-B.; Lee, C.-H. Adsorption Characteristics of Hydrogen Mixtures in a Layered Bed: Binary, Ternary, and Five-Component Mixtures. *Ind. Eng. Chem. Res.* **2001**, *40* (3), 868−878.
(52) Xiao, J.; Peng, Y.; Bénard, P.; Chahine, R. Thermal effects on breakthrough curves of pressure swing adsorption for hydrogen purification. *Int. J. Hydrogen Energy* **2016**, *41* (19), 8236−8245.
(53) Ribeiro, A. M.; Grande, C. A.; Lopes, F. V. S.; Loureiro, J. M.; Rodrigues, A. E. A parametric study of layered bed PSA for hydrogen purification. *Chem. Eng. Sci.* **2008**, *63* (21), 5258−5273.
(54) Ribeiro, A. M.; Grande, C. A.; Lopes, F. V. S.; Loureiro, J. M.; Rodrigues, A. E. Four beds pressure swing adsorption for hydrogen purification: Case of humid feed and activated carbon beds. *AIChE J.* **2009**, *55* (9), 2292−2302.
(55) Yang, J. Y.; Lee, C. H.; Chang, J. W. Separation of hydrogen mixtures by a two-bed pressure swing adsorption process using zeolite 5A. *Ind. Eng. Chem. Res.* **1997**, *36* (7), 2789−2798.
(56) Chen, Y.; Ahn, H. Optimization Strategy for Enhancing the Product Recovery of a Pressure Swing Adsorption through Pressure Equalization or Co-current Depressurization: A Case Study of Recovering Hydrogen from Methane. *Ind. Eng. Chem. Res.* **2023**, *62* (12), 5286−5296.
(57) Lu, Z. P.; Loureiro, J. M.; Levan, M. D.; Rodrigues, A. E. Pressure Swing Adsorption Processes - Intraparticle Diffusion Convection Models. *Ind. Eng. Chem. Res.* **1993**, *32* (11), 2740−2751.

https://doi.org/10.1021/acs.iecr.3c04532
Ind. Eng. Chem. Res. 2024, 63, 6333−6346